



**HAL**  
open science

## Deactivation mechanism and regeneration study of Zn/HZSM-5 catalyst in ethylene transformation

Aurélien Bonnin, Yannick Pouilloux, Vincent Coupard, Denis Uzio, Ludovic  
Pinard

► **To cite this version:**

Aurélien Bonnin, Yannick Pouilloux, Vincent Coupard, Denis Uzio, Ludovic Pinard. Deactivation mechanism and regeneration study of Zn/HZSM-5 catalyst in ethylene transformation. *Applied Catalysis A: General*, 2021, 611, pp.117976. 10.1016/j.apcata.2020.117976 . hal-03159790

**HAL Id: hal-03159790**

**<https://ifp.hal.science/hal-03159790>**

Submitted on 3 Feb 2023

**HAL** is a multi-disciplinary open access archive for the deposit and dissemination of scientific research documents, whether they are published or not. The documents may come from teaching and research institutions in France or abroad, or from public or private research centers.

L'archive ouverte pluridisciplinaire **HAL**, est destinée au dépôt et à la diffusion de documents scientifiques de niveau recherche, publiés ou non, émanant des établissements d'enseignement et de recherche français ou étrangers, des laboratoires publics ou privés.



Distributed under a Creative Commons Attribution - NonCommercial 4.0 International License



36

37

### 38 **Introduction**

39 Catalytic Cracking (FCC) is a key process in petroleum refinery. This  
40 technology yields light olefins, e.g. ethylene, propylene, butylenes as by-products that  
41 are sent to a gas recovery unit. Recovered propylene/butylenes are processed in  
42 alkylation or oligomerization facilities to produce additional high-octane gasoline,  
43 while unrecovered light olefins (dry gas), including ethylene, are routed to the refinery  
44 fuel system. The quantity of light olefins burned in the fuel system can become even  
45 more significant as FCC catalysts are employed. The consumption of a potentially  
46 high-value product for low-value energy purposes can be avoided by developing  
47 technologies to convert ethylene into desirable products such as propylene and  
48 aromatics. [1-2]

49 ZSM-5 doped with zinc has proven as suitable catalyst for the aromatization of  
50 ethylene at high temperature (500 °C), which mainly yields BTX, light olefins  
51 (propylene, butenes) and hydrogen. [3-6]. Zn impregnation on H/ZSM-5 zeolite  
52 increases the concentration of Lewis acid sites (LAS) and concomitantly decreases  
53 that of Brønsted acid sites (BAS). [4] A high LAS/BAS ratio improves the initial yield  
54 of BTX. [7]

55 The main issue for the industrial development of ethylene aromatization is to  
56 mitigate catalyst deactivation. [1-2, 7] There are many reasons for the deactivation of a  
57 bifunctional catalyst such as Zn/HZSM-5 [8], e.g. loss of metal species from the  
58 catalyst under reducing conditions [9,10], and/or the coking which may poison or  
59 block access to active sites. [11-13]. The deactivation rate also depends on the balance  
60 between the two functions. Zhang et al. suggested that the balance between the Lewis

61 and Brønsted acid sites is the key property to obtain both high aromatics yield and  
62 high catalyst stability; the suitable LAS/BAS ratio is around of 1. [7]

63

64 This study is devoted to the understanding of the impact of the molar ratio of  
65 Zn active sites and  $H^+$  on the catalyst stability and on the nature and toxicity of coke.  
66 More than 15 catalysts, with a Zn/ $H^+$  molar ratio ranging from 0 (H-ZSM5) to 1.8  
67 (Zn/H-ZSM5), were prepared by wet impregnation, characterized by different probe  
68 molecules ( $N_2$ , pyridine), and tested in ethylene transformation at 500 °C. The  
69 deactivating species and deactivated/regenerated catalysts have also been be  
70 characterized.

## 71 1. Experimental part

72 **Material:** Three series of Zn-containing catalyst were prepared from three commercial  
73 zeolites (Zeolyst) with a global Si/Al molar ratio of 15 (CBV 3042E), 40 (CBV 8014)  
74 and 75 (CBV 1502). The CBV 3042E and CBV 8014 under ammonium form were  
75 calcined under air at 500°C for 12 h. Zn-containing zeolites were prepared by wet  
76 impregnation by stirring protonic zeolite with an aqueous solution of  $Zn(NO_3)_2 \cdot 6H_2O$   
77 at 60 °C for 30 min, in the proportion of 1g of zeolite per 10 mL of  $Zn(NO_3)_2 \cdot 6H_2O$   
78 solution. The concentration of the precursor salt solution ranges between 0.008 and  
79  $0.12 \text{ mol L}^{-1}$  depending of the zinc loading expected. Then, the samples were dried at  
80 120 °C for 12 h without preliminary filtration and calcined at 500 °C under air (60  
81  $\text{mL} \cdot \text{min}^{-1}$ ) for 12 h.

82 **Catalytic test:** A typical catalytic test for the ethylene conversion (Air Liquid, > 99%)  
83 was performed at atmospheric pressure in a fixed-bed continuous flow quartz reactor  
84 at 500 °C with a  $N_2$ /reactant molar ratio of 19, which correspond to an ethylene partial

85 pressure of 0.005 MPa. The length and diameter of the catalytic bed are 13 and 6 mm,  
86 respectively. No pre-bed of inert material was used. In standard condition the weight  
87 gas hourly space velocity WHSV (g of injected C<sub>2</sub>H<sub>4</sub> per hour and per g of catalyst)  
88 was 2 h<sup>-1</sup>, and the gas hourly space velocity was 13 300 h<sup>-1</sup> which corresponds to a  
89 short contact time of 7.5 10<sup>-5</sup> h. Before testing, 200 mg of catalyst was compacted,  
90 crushed and sieved to obtained homogeneous particles (0.2-0.4 mm). Samples were  
91 pre-treated at 500 °C (5 °C min<sup>-1</sup>) under nitrogen flow (100 mL.min<sup>-1</sup>) for 1 h. The  
92 trace heated lines between reactor and GC are 200 °C. The gaseous products and  
93 hydrogen were analysed online by a Varian CP-3800 gas chromatograph equipped  
94 with a FID detector using a fused silica J&W GS-Gaspro capillary column (60 m x  
95 0.32 mm x 4 µm) and a TCD using a J&W PoraPLOT Q-HT capillary column (25 m x  
96 0.53 mm x 20 µm). GC equipment was calibrated with a gas mixture (C<sub>1</sub> to C<sub>6</sub> in N<sub>2</sub>,  
97 800 ppm each compound, Air liquid).

98 The standard deviation of the catalytic data is assessed to 2%. (**Fig. SI.1**)

99 ***Characterization of the fresh and spent catalysts:*** The elemental composition of the  
100 bifunctional catalysts (Si, Al, Zn) was determined before and after ethylene  
101 transformation using inductively coupled plasma-atomic emission spectroscopy (ICP-  
102 AES) on an Optima 2000 DV (Perkin-Elmer). The samples (30-40 mg) were  
103 mineralized by three successive acid attacks by HNO<sub>3</sub> (69 vol. %), HCl (37 vol. %)  
104 and HF (40 vol. %) in the proportion 4/2/2 mL, respectively. The mineralization was  
105 carried out in sealed vessels at 180 °C under an autogenous pressure of 2.0 MPa for 45  
106 min using a microwave oven (Anton-Parr Multiwave Pro). Finally, 12 mL of a  
107 saturated solution of H<sub>3</sub>BO<sub>4</sub> was added to the sample. Textural properties were  
108 determined by sorption measurements of nitrogen at -196 °C, using a Micromeritics  
109 ASAP 2000 gas adsorption analyzer. Prior to measurement, samples were outgassed at

110 90 °C for 1 h and 350 °C for 4 h both with a heating ramp of 10 °C min<sup>-1</sup>. Coked  
111 samples were outgassed at 90 °C for 1 h and 150 °C for 1 h to avoid coke desorption.  
112 The microporous volumes ( $V_{\text{micro}}$ ) were calculated using the  $t$ -plot method and the  
113 total pore volume was calculated at  $p/p_0 = 0.98$ . The nature, concentration of acidity  
114 were studied by using pyridine as a probe molecule followed by infrared spectroscopy  
115 (FTIR) through a Nicolet 5700 apparatus with 2 cm<sup>-1</sup> optical resolution. Before  
116 analysis, the catalyst was pressed for 2 s at 0.5 ton into a self-supporting wafer (2 cm<sup>2</sup>)  
117 and pretreated from 20 °C to 500 °C under nitrogen flow (100 mL min<sup>-1</sup>). The fresh  
118 and regenerated catalysts were then out-gassed (10<sup>-5</sup> bar) for 1 h at 350 °C, after which  
119 finally an IR spectrum was taken, while on spent catalyst the pretreatment  
120 temperature was 150 °C, with a heating ramp of 10 °C min<sup>-1</sup>. Then, the sample was  
121 cooled to 150 °C and exposed to 1.5 mbar pyridine pressure for 5 min and then  
122 outgassed (10<sup>-5</sup> bar) for 1h in order to eliminate the physisorbed pyridine. The FTIR  
123 spectrum was taken at 25 °C. The Beer-Lambert-Bouguer law was applied in the form  
124  $[H^+] \text{ or } [L] = \left(\frac{S}{m}\right) \frac{A}{\epsilon}$ , where  $[H^+]$  and  $[L]$  is the concentration of Brønsted and Lewis  
125 acid sites ( $\mu\text{mol g}^{-1}$ ),  $A$  denotes the integrated absorbance of the corresponding IR  
126 bands (1545 and 1455 cm<sup>-1</sup>), which is normalized to zeolite wafer density (ratio of the  
127 wafer weight (mg) to wafer surface (cm<sup>2</sup>), and  $\epsilon$  is the integrated molar adsorption  
128 coefficient measured at 25 °C:  $\epsilon_{1545} = 1.13$  and  $\epsilon_{1454} = 1.28$  cm mol<sup>-1</sup>. [14] The  
129 calibration curves were obtained on a MFI (Si/Al=27) and a  $\gamma$  Al<sub>2</sub>O<sub>3</sub> by adding to the  
130 IR cell a known amount of pyridine vapor from gas admission compartment (0.9122  
131 cm<sup>3</sup>). All the reported FTIR spectra recorded at 25 °C are normalized to a wafer  
132 density (mg cm<sup>-2</sup>).

133 The coke content and the temperature of coke oxidation ( $T_{ox}$ ) were obtained with  
134 a SDT Q600 TA thermogravimetric analyser under a flow rate of  $100 \text{ mL min}^{-1}$  of air  
135 up to  $900^\circ\text{C}$ .

136 **Coke extraction** [15]: In order to release molecules trapped in zeolite pores, the spent  
137 catalyst was dissolved in 51 vol % hydrofluoric acid solution at room temperature  
138 during 20 min. HF was neutralized by a boric acid solution and sodium hydrogen  
139 carbonate. Coke molecules were extracted by liquid-liquid extraction with  $\text{CH}_2\text{Cl}_2$ .  
140 After total evaporation of the solvent, the solid is dissolved in dichloromethane in  
141 order to obtain a concentration into soluble coke of  $20 \text{ mg L}^{-1}$ . The solution is  
142 analyzed using a GC-MS (Thermoelectron DSQ). The low temperature of treatment  
143 by HF, the short contact time of the acid solution and the coke components as well as  
144 the very small contact area between mineral and organic phases allow to avoid any  
145 change of coke composition.

## 146 **2. Results and discussion**

147 **Characterizations of the bifunctional catalysts.** Three series of bifunctional  
148 catalysts were prepared by wet impregnation from HZ15, HZ40 and HZ75 commercial  
149 zeolites with a Zn loading ranging from 0.3 to 8.1 wt. %. Zn based catalysts are named  
150 by  $x\text{Zn}_y$  where x is the zinc content and y the Si/Al molar ratio.

151 The TPR study on 2.1Zn40 shows no reduction. Indeed, Biscardi et al. have  
152 shown that  $\text{Zn}^{2+}$  cations in ion-exchanged 1.07Z14.5 do not reduce even at  $877^\circ\text{C}$  and  
153 ZnO crystals begin to reduce to Zn metal and sublime around  $480^\circ\text{C}$  in flowing  
154 hydrogen. [16] It should be noted that a pretreatment of 2.1Zn40 under  $\text{H}_2$  at  $500^\circ\text{C}$   
155 has no impact on activity, selectivity and stability suggesting that the oxidation state of  
156 Zn is +2.

157 The textural properties of the commercial zeolites features micropore volumes  
158 between 0.15-0.18 cm<sup>3</sup> g<sup>-1</sup>, which is typical value for ZSM-5 zeolite [17]. For the  
159 HZ15 and HZ75 catalyst series, the microporous volume is only slightly affected by  
160 high Zn loadings, probably due to the deposition of a small amount of subnanometric  
161 (ZnO)<sub>n</sub> particles in the micropores. On the other hand, for the series HZ40, V<sub>micro</sub>  
162 decreases with increasing Zn content, which suggests that on this zeolite, which  
163 features internal defects, the Zn oxide species (ZnO) may be located in the  
164 microcavities formed by the hydroxyl nests. The incorporation of the metal into the  
165 framework of HZ40 is confirmed by UV-vis adsorption spectroscopy (**Figure 1**),  
166 which shows an adsorption band at about 265 nm. Zhang et al. to Zn attributed this in  
167 the zeolite framework [18]. Incorporation of Zn into the MFI framework can be done  
168 by isomorphic substitution by healing silanol nests. [19-20] An adsorption band at  
169 about 370 nm<sup>-1</sup>, which corresponds to the band gap width of macrocrystalline ZnO  
170 appears when the Zn loading exceeds 1.4 wt.%.

171 TEM images (**Figure 2**) clearly show that some (ZnO)<sub>n</sub> particles cover the  
172 external surface of the HZ40 zeolite. On the 3.6Zn40 catalyst, their size (9.1 nm) is  
173 twelve times larger than the diameter of the larger void volume within the MFI  
174 framework, i.e. 0.70 nm in the channel intersections. It appears that Zn cations, which  
175 do not exchange with zeolite protons, precipitates as (ZnO)<sub>n</sub> species and grow on the  
176 outer surface during the solvent evaporation step. Their size therefore depends in part  
177 on the exchange capacity of the zeolite. The (ZnO)<sub>n</sub> particles in 4.1Zn15 and 2.7Zn75  
178 were measured and are of 6.8 and 14.8 nm, respectively.

179 **Figure 3** compares the infrared spectra in the OH stretching region of the three  
180 catalyst series. HZ75 has two IR bands: an intense band at 3610 cm<sup>-1</sup> (± 2) attributed  
181 to the bridged hydroxyl groups (Si-O(H)-Al) and an asymmetric band at 3740 cm<sup>-1</sup>

182 ascribed to the terminal silanol groups on the external surface. On HZ40, the shoulder  
183 at  $3726\text{ cm}^{-1}$  corresponds to Si-OH located on the intraparticle defects and is  
184 correlated with the broad band centred at  $3470\text{ cm}^{-1}$ , which is assigned to the hydroxyl  
185 nests. The intensities of the bridged OH-band of the three catalysts series decrease  
186 partially (**Figure 3b**), even with a Zn content in solution two to three times higher than  
187 their exchange capacity, which is calculated assuming a Zn/Al molar ratio of 0.5 (1/2),  
188 i.e. 0.7, 1.4 and 3.4 wt. % on HZ75, HZ40 and HZ15, respectively.

189 Pyridine adsorbed on zeolites leads to characteristic bands at  $1546$  and  $1454\text{ cm}^{-1}$   
190 which appear due to protonated pyridine at Brønsted acid sites (BAS) and pyridine  
191 coordinated to Lewis acid sites (LAS), respectively. The concentration of pyridinium  
192 ions decreases rapidly with Zn addition, then very slightly with further metal  
193 incorporation (**Figure 4a**). The concentration of the Zn-based Lewis acid sites follows  
194 the reverse trend as the neutralization of the Brønsted acid sites (**Figure 4b**). The ratio  
195 between the neutralized BAS and created LAS is two (**Figure 4c**). The neutralization  
196 of the one protonic site leads to the creation of one Zn Lewis acid site which  
197 coordinates two pyridine molecules. The balance between Zn Lewis and Brønsted acid  
198 sites (given by the ratio of  $Zn_{\text{Lewis}}/H^+$ ) is higher than 5 (**Table 1**).

199 **Kinetic of deactivation.** **Figure 5** shows the ethylene conversion at  $500\text{ }^\circ\text{C}$  under  
200 atmospheric pressure against time-on-stream (TOS). HZ15 converts ca 60 % of  
201 reactant with almost no deactivation during 280 min. Whereas on HZ40 and HZ75,  
202 less than 2% of ethylene is converted, which is apparently in direct contradiction with  
203 the results of numerous studies [21-27]. The observed low activity can be ascribed to  
204 the severe operating conditions that were employed. Indeed, high temperature [24],  
205 low partial pressure of the olefin [24, 26-27] and short contact times hinder the  
206 oligomerization reaction. The activity of HZ15 could be due to the high density of the

207 Brønsted acid sites. The wet impregnation of zinc on zeolite leads to an increase in  
208 conversion (except on 0.7Zn15) followed by deactivation, which increases with the  
209 zinc loading. 2.1Zn40 catalyst appears to be less active in the transformation of  
210 ethylene than HZ15 zeolite. Hence, the initial decline in activity of HZ15 after the  
211 addition of Zn is consistent with the neutralization of the very active aluminium pairs.

212 The catalyst deactivation constant ( $k_D, s^{-1}g_{cata}^{-1}$ ) can be assessed from the time-on-  
213 stream (TOS) theory by a simple exponential law, which corresponds to a  
214 deactivation order of 1:  $a_{280} = a_{10}e^{-k_D t}$  with  $a_t$  and  $a_{10}$  corresponding to activities  
215 on spent and fresh catalysts, respectively. It is worth noting that the TOS theory is  
216 based on the assumption that the concentration of active sites is simply a time-  
217 dependent power function of the remaining concentration of active sites and that all  
218 have the same strength. [28] The deactivation curves fit the exponential law very well  
219 (**Fig. SI. 2**); the catalyst deactivation constant ( $k_D$ ) are shown in **Table 1**. For each  
220 catalyst series; the kinetic deactivation constant depends on the concentration of  
221 Brønsted acid sites (**Figure 6a**), on that of Zn-Lewis acid sites (**Figure 6b**). The only  
222 variable with which a correlation with  $k_d$  can be observed for all the catalyst series is  
223 the Lewis/Brønsted ratio (**Figure 6c**). Indeed, the dependence of  $k_D$  with LAS or BAS  
224 follow different trends for each Si/Al ratio. This correlation indicates that deactivation  
225 occurs *via* a bifunctional mechanism.

226 The loss of activity between 10 and 280 min ( $a_{280}/a_{10}$ ) increases unexpectedly  
227 with decreasing BAS concentration. For each catalyst series, the higher the  
228 concentration of Brønsted acid sites the higher the catalyst stability. In addition, at iso-  
229 concentration of the acid sites, the lower the Si/Al zeolite ratio the lower the residual  
230 activity. (**Figure 7a**). In contrast,  $a_{280}/a_{10}$  decreases with increasing of the  
231 concentration of Zn-Lewis acid sites (**Figure 7b**) and at iso-concentration of  $Zn_{Lewis}$

232 the lower the Si/Al zeolite ratio the lower the residual activity. Yet, the loss of activity,  
233 regardless of the Si/Al ratio, follows an exponential law of the  $Zn_{Lewis}/H^+$  ratio (**Figure**  
234 **7c**):  $\phi = \frac{a_{280}}{a_{10}} = 0.953e^{-0.53\frac{[Zn_{Lewis}]}{[H^+]}}$ . Hence, the balance between Lewis and Brønsted  
235 acid sites is a good descriptor for predicting catalyst stability.

236 **Kinetic of coking.** Deactivation does not result from a loss of Zn by sublimation  
237 since the metal content after 280 min of reaction is identical to that of the fresh  
238 catalyst (**Fig SI.3**). Deactivation is only due to coking. **Table 1** reports the coke  
239 content (wt. % C) on the catalysts after 280 minutes of reaction. The carbon content,  
240 which is low on protonic catalysts, (1.4 wt. % on HZ15) reaches up to 7.5 wt. % on  
241 bifunctional catalysts.

242 The deactivating effect of coke on the kinetics was studied on the 3.4Zn15  
243 catalyst. The coke formation on the bifunctional catalyst is slow and follows a linear  
244 regression ( $\sim 0.01 \text{ g}_{\text{coke}} \text{ g}_{\text{cata}}^{-1} \text{ h}^{-1}$ ) with an intersection point at 1.7 wt. % (**Figure 8a**).  
245 This value is close to the coke content obtained on protonic zeolite. The loss of  
246 catalytic activity ( $\Phi = \frac{a_{280}}{a_{10}}$ ) fits with an exponential dependence on the coke content  
247 ( $C_c$ ):  $\Phi = C_Z e^{-\alpha_k C_c}$  (**Figure 8b**). This deactivation function is frequently used to  
248 describe the loss of activity [12, 29-31]. The constant in the exponential,  $\alpha_k$  in (wt. %<sup>-1</sup>)  
249 <sup>1</sup>), is the so-called coking constant.  $\alpha_k$  is equal to 0.307 wt. %<sup>-1</sup>, which is ca 6 times  
250 lower than the coke formation in the catalytic cracking of 2,2,4 trimethylpentane on a  
251 USY zeolite at 480 °C, but  $\alpha_k$  is in the same range as that of hydride transfer (0.653),  
252 protonation and PCP isomerization (0.148),  $\beta$  scission (t-t) (0.407) and protolytic  
253 scission (0.445). [32] The higher value of deactivation constant ( $\alpha_k$ ) for coke  
254 formation in FAU zeolite is certainly due to the presence of supercages. The  
255 deactivation function has a pre-exponential factor (A), which means that one part of

256 coke is trapped on the zeolite without significant impact on catalyst activity. On the  
257 HZ15 zeolite, the low coke content (1.4 wt. %) has almost no impact on the catalyst  
258 stability. Some of coke molecules could simply be trapped by silanol groups without  
259 impact on catalyst activity [33] and Brønsted acidity (**Table 1**). Subtracting of the total  
260 coke with that measured on the protonic zeolite, gives a pre-exponential factor of 1  
261 (**Figure 8b**) and in the case of the coking rate a straight line through the origin (**Figure**  
262 **8a**). Hence, there are two types of coke: a spectator coke (minority) and deactivating  
263 coke (majority). The deactivation function ( $\phi$ ) can be modelled by an exponential law  
264 of the coke content or the balance between the Lewis and Brønsted acid sites. This  
265 indicates that these two parameters are related, which suggests that deactivation occurs  
266 by poisoning of the Lewis and Brønsted dual sites.

267 **Figure 9** shows the infrared spectra in the OH stretching region of the 3.4Zn15  
268 catalyst after different reaction time. After 30 minutes of reaction, the intensity of the  
269 silanol band decreases significantly then remains constant, indicating their role as a  
270 coke trap. [33] The intensity of Si-O(H)-Al decreases continuously with increasing  
271 coke content, while that of the hydroxylated extraframework species seems much less  
272 sensible to coke deposits.

273 **Figure 10** displays for the 3.4Zn15 catalyst, the losses of Brønsted and Lewis acid  
274 sites and micropore volumes as a function of time and coke content. The loss kinetics  
275 of Brønsted acid sites is proportional to reaction time (**Figure10a**) and coke content  
276 (**Figure 10b**) when coke trapped on silanol groups is subtracted (**Fig.SI.4**). The loss  
277 kinetics of micropore volumes follows the same trend, while the loss kinetics of Lewis  
278 acid sites begins after a slightly higher coke content ( $4-1.4 = 2.6$  wt. %). The increase  
279 of LAS concentration suggests that some coke precursors present a Lewis acid site  
280 character. Indeed, Cerqueira et al. observed that the coke deposit on USHY zeolite

281 leads to a decrease of the concentration of protonic sites, while that of Lewis sites  
282 increases after coking. [34]

283 **Deactivation and selectivity.** **Figure 11** compares, as a function of ethylene  
284 conversion, the molar yields of H<sub>2</sub>, CH<sub>4</sub>, ethane, propylene, butenes, and aromatics  
285 obtained after 10 and 280 minutes. On fresh HZ15 zeolite, oligomerization-cracking  
286 reaction occurs, yielding propylene and butane. Aromatics result from the  
287 transformation of naphthenes by dehydrogenation and hydride transfer reactions,  
288 producing hydrogen and paraffins (mainly ethane), respectively. CH<sub>4</sub> results more  
289 from the dealkylation reaction of toluene and xylene than from  $\alpha$ -scission of olefins.  
290 (The operating conditions favour the dealkylation reaction rather than the alkylation  
291 reaction).

292 Despite high yields of coking molecules such as light olefins as well as a high  
293 temperature and high density of acidic sites, the formation of coke remains low (1.4%  
294 wt. %) even after a long period of operation. Catalyst deactivation is slow. The  
295 operating conditions of ethylene aromatization such as a low contact time and mainly  
296 a low partial pressure of ethylene ( $P_{C_2H_4} = 5.2 \cdot 10^{-3}$  MPa, do not promote the coke  
297 formation by the conventional acid mechanism.

298 The wet impregnation of Zn completely changes the selectivity of the acid  
299 catalyst. C<sub>4</sub>H<sub>8</sub> is clearly a primary product, while CH<sub>4</sub>, C<sub>3</sub>H<sub>6</sub>, H<sub>2</sub> and aromatics  
300 composed of benzene (B), toluene (T) and also xylene (X) and ethylbenzene (EB), are  
301 secondary products. These products could practically be considered as primary  
302 products (**Figure 11**) because they are produced simultaneously from a very low  
303 conversion, ca 2% (extrapolated value). Hydrogen resulting from the dehydrogenation  
304 of naphthenes or olefinic naphthenes, is also consumed at high conversion through the  
305 hydrogenation of olefins (mainly ethylene) into light alkanes. The hydrogenation of

306 ethylene has a direct impact on the yield of aromatics, limiting or even decreasing it  
307 when a large part of ethylene is hydrogenated.

308 In the absence of hydrogenation side-reactions ( $X < 30\%$ ), the coke content is  
309 proportional to the initial aromatics yield ( $X_{Ar}$ ), but when  $H_2$  begins to be consumed  
310 for ethane formation, the coke content decreases more on the series 40 than the series  
311 15, resulting in lower  $X_{Ar}$ . (**Figure 12**). The lower coke content could be attributed to  
312 the hydrogenation of coke precursors [21-22], since hydrogenation reactions take  
313 place at high conversion. The proportionality suggests that the coke maker molecules  
314 on bifunctional catalysts are aromatics.

315 The catalyst deactivation has no impact on the selectivity as shown in **Figure**  
316 **11**. It should be noted that the selectivity into hydrogenated products is slightly higher  
317 on spent catalysts despite a lower hydrogen yield, indicating that coke deposition has a  
318 greater impact on the dimerization sites than on the hydrogenation sites.

319 **Characterization of the deactivating species.** The bands of carbonaceous  
320 compounds deposited on catalysts are observed on two IR spectra domains: i) 2700-  
321 3100  $cm^{-1}$  (**Figure 13**): CH stretching modes of aromatic and paraffinic groups, ii)  
322 1300-1700  $cm^{-1}$  (**Figure 14**): CC stretching modes of unsaturated (olefin, polyenyl,  
323 aromatic and polyaromatic) groups and CH bending of paraffinic groups. The band at  
324 2935  $cm^{-1}$  is assigned to the asymmetric stretching mode of  $CH_2$  groups, and 2957 and  
325 2864  $cm^{-1}$  correspond to the symmetric stretching mode of  $CH_2$  and  $CH_3$ . The  
326 intensities of the bands of coke increase with the Zn loading on all series, but when  
327 hydrogenation side-reactions occur especially on series 15 and 40, their intensities  
328 decrease significantly, which indicates a lower degree of alkyl groups on the aromatic  
329 rings.

330 The attribution of bands in region between 1300-1800  $\text{cm}^{-1}$  is more complex, as in  
331 this region appear different stretching modes of C=C condensed and non-condensed  
332 aromatics; and also bending vibrations of CH. Regardless of the coke content, all spent  
333 catalysts exhibit bands at 1591, 1470, 1426 and 1371  $\text{cm}^{-1}$ , which can be attributed to  
334 coke molecules with a number of aromatic rings higher than 3. [35] It should be  
335 mentioned that the IR spectra are recorded on catalysts which have been operated for  
336 280 min; this long time allows the growth of coke precursors into polyaromatic  
337 compounds. The intensities of the bands of coke in this region are proportional to the  
338 coke content (**Figure SI. 5**) which reaches a plateau at ca 6 wt.% , probably due to  
339 signal saturation.

340 The composition of coke trapped inside the zeolite pore is determined on 2.1Zn40  
341 and 5.6Zn40 by mineralizing the zeolite matrix and subsequently analyzing the  
342 organic leftovers by liquid-liquid extraction with  $\text{CH}_2\text{Cl}_2$ . GC/MS analysis (**Figure SI.**  
343 **6**) shows that the coke composition on both catalysts consists of polyaromatic  
344 compounds such as naphthalene, anthracene, phenanthrene, pyrene and  
345 benzo[e]pyrene, which are alkylated by only two or three methyl groups, When the  
346 hydrogenation side reaction occurs on the 5.6Zn40 catalyst the number of methyl  
347 groups is limited to one. The degree of alkylation of coke molecules is relatively low  
348 compared to that observed on coke molecules formed during the transformation of  
349 alcohols at 350  $^{\circ}\text{C}$ , with more than 10-12 alkyl groups. [33,35] The low coke content  
350 on the catalysts, despite a high reaction time, could be due to a low degree of  
351 alkylation of the coke molecules. Indeed, the mechanism of coke formation occurs by  
352 alkyl side chain growth. [15]

353 **Characterization of the spent catalysts.** The residual micropore volume and the  
354 Brønsted and Lewis acid sites remaining after 280 minutes of reaction are reported for  
355 the three catalyst series in **Table 1**.

356 The volume apparently occupied by coke ( $V_a$ ), deduced from the physisorption  
357 measurement, is roughly proportional to its content (**Figure 15a**). The volume really  
358 occupied by the coke molecules ( $V_R$ ) can be assessed by assuming that the density of  
359 coke is close to that of phenanthrene, anthracene pyrene and benzo[e]pyrene: 1.18,  
360 1.25, 1.27 and 1.24 g cm<sup>-3</sup> respectively. Therefore, the coke density in this study is  
361 chosen to be 1.25 g cm<sup>-3</sup>. A  $V_R/V_A$  value of 0.56, (**Figure 15b**) indicates a blockage of  
362 access of the adsorbate molecules to a part of the microporosity unoccupied by the  
363 coke molecules. Indeed, the coke molecule trapped at the channel intersections of the  
364 MFI zeolite completely blocks their access, without occupying the totality of their  
365 volume. The loss of micropore volume results in a progressive deactivation of the  
366 bifunctional catalyst (**Figure 15c**), indicating that the deactivation occurs by poisoning  
367 and not by pores blocking as with mordenite zeolites. [36]

368 **Figure 16** shows the proportion of the Brønsted and Lewis sites neutralized by  
369 coke:  $1 - \frac{[H^+]_{280}}{[H^+]_0}$  (**Figure 16a**) and  $1 - \frac{[PyL]_{280}}{[PyL]_0}$  (**Figure 16b**), respectively. The  
370 proportion of protonic sites neutralized rises rapidly with the deposition of coke, but  
371 after only 2 wt. %, it remains constant and partial (70%) despite the increase of the  
372 coke content and substantial pore blocking ( $V_R/V_A = 0.56$ ). This apparent  
373 disagreement between quantification of residual acid site and microporous volume  
374 analysis, can be easily explained by considering that the coke molecules which are  
375 trapped at the channels intersections of MFI zeolite completely block their access,  
376 without occupying the totality of the volume. [37] The proportion of Lewis acid sites  
377 neutralized by coke is less evident (**Figure 16b**), due to the proportion of coke

378 poisoning the Brønsted acid sites and the presence of Zn-Lewis acid sites. On the  
379 protonic zeolites, the number of Al-Lewis acid probed by pyridine is higher after coke  
380 deposits (**Table 1**), which means that some coke molecules are able to coordinate  
381 pyridine. Nevertheless, it appears as main trend that the proportion of neutralized Zn-  
382 Lewis acid sites increases with increasing coke content, causing catalyst deactivation  
383 (**Figure 15d**). The deactivation results in the neutralization of the Zn-Lewis acid sites,  
384 which are located in the zeolite micropores.

385 **Catalyst regeneration.** The coke combustion occurs between 400 °C and 700 °C.  
386 **Figure 17** shows the temperatures at which 50 (T50) and 90 % (T90) of coke is burnt  
387 as a function of the concentration of Brønsted (**Figure 17b**) and Lewis Zn (**Figure**  
388 **17a**) acid sites, the  $Zn_{Lewis}/H^+$  molar ratio (**Figure 17c**), the micropore volume of the  
389 spent catalyst (**Figure 17d**) and coke content (**Figure 17e**). T90 is almost identical on  
390 all spent catalysts (i.e. 630-650 °C), in contrast to T50, which is between 465-585 °C.  
391 The coke combustion depends mainly on the accessibility of oxygen to the coke rather  
392 on the redox and acidic properties of the bifunctional catalyst. Zn metal does not  
393 participate to the coke combustion. The accessibility and coke content are strongly  
394 related.

395 The regeneration was studied on 3.6Zn40 catalyst through two reaction-  
396 regeneration cycles (**Figure 18**). The regeneration was carried out under mild  
397 conditions, i.e. at the same temperature as the ethylene transformation temperature  
398 (500 °C) for 12 h. Despite the low temperature used, all coke molecules were  
399 removed. But only a portion of the acidic properties are recovered after regeneration.  
400 The concentration of LAS is lower than on the fresh catalyst in favour of a slight  
401 increase of BAS (**Table 2**). This impacts the performance of the catalyst as the

402 catalytic activity is reduced. In addition, a second regeneration step leads to a radical  
403 change in acidic properties, mainly for Lewis acid site and slight loss of Zn content.

404 Despite mild regeneration conditions; deactivation is partially irreversible, due  
405 to modification of acidity during coke combustion. In order to verify this assumption a  
406 milder regeneration process should be used, such as non-thermal plasma. [38-39]

## 407 **Conclusion**

408 The selective transformation of light olefins into aromatics, which are more  
409 valuable and versatile feedstocks for the chemical industry, is one of the major  
410 challenges in petrochemistry. ZSM-5 doped with zinc is a proven catalyst for the  
411 aromatization of ethylene at high temperature (500 °C). Yet, the coking is the greatest  
412 drawback of this reaction, as all the conditions are present to promote its formation:  
413 confined acid sites, presence of aromatics and light olefins (coke precursors) and high  
414 temperature. However, Brønsted acid sites, even with an acidity exalted by the  
415 presence of extraframework species, yield relatively low coke formation. The coking  
416 is favoured by the presence of Zn-Lewis acid sites. However, its rate remains rather  
417 limited due to the low degree of alkyl groups on the aromatic rings, which impedes the  
418 growth of coke. Therefore, reducing diffusion path length by zeolite hierarchization  
419 seems very promising to mitigate coke formation. The catalyst stability depends on the  
420 balance between the Zn-Lewis and Brønsted acid sites and the yield into desired  
421 products: hydrogen and aromatics on the content of Zn species, but when its  
422 concentration is high hydrogen is consumed. Hence, the best compromise for an active  
423 and stable catalyst in ethylene aromatization consists to have a moderate balance  
424 between Zn-Lewis and Brønsted acid sites, around 1.5 and 2. In addition, the  
425 development of this process requires a fine management of the regeneration stage.

426 **Acknowledgment**

427 The authors gratefully acknowledge IFPEN for the financial support. The authors  
428 acknowledge financial support from the European Union (ERDF) and "Région  
429 Nouvelle Aquitaine". Aurelien Bonnin thanks "Ministère de l'enseignement supérieur,  
430 de la recherche et de l'innovation" for Ph.D grant.

431 **REFERENCE**

- 432 [1] C. P. Nicholas, A. Bhattacharyya, D. E. Mackowiak, Process for  
433 oligomerization of dilute ethylene, Patent US/2013 8,575,410 B2.
- 434 [2] W. M. Cross, D. T. Shay, R. C. Zhang, F. Zhang, Process for oligomerization  
435 of dilute ethylene, Patent US/2017 004446 A1.
- 436 [3] Chen, X.; Dong, M.; Niu, X.; Wang, K.; Chen, G.; Fan, W.; Wang, J.; Qin, Z.  
437 Influence of Zn species in HZSM-5 on ethylene aromatization, *Chin. J. Catal.*,  
438 **2015**, *36*, 880-888.
- 439 [4] Coqueblin, H.; Richard, A.; Uzio, D.; Pinard, L.; Pouilloux, Y.; Epron, F.  
440 Effect of the metal promoter on the performances of H-ZSM5 in ethylene  
441 aromatization, *Catal. Today*, **2017**, *289*, 62-69.
- 442 [5] Hulea, V. Toward platform chemicals from bio-based ethylene: heterogeneous  
443 catalysts and processes, *ACS Catal.*, **2018**, *8*, 3263-3279.
- 444 [6] Gao, J.; Wei, C.; Dong, M.; Wang, G.; Li, Z.; Qin, Z.; Wang, J.; Fan, W.  
445 Evolution of Zn species on Zn/HZSM-5 catalyst under H<sub>2</sub> pretreated and its  
446 effect on ethylene aromatization, *ChemCatChem*, **2019**, *11*, 3892-3902.
- 447 [7] Zhang, C., Kwak, G., Lee, Y-J., Jun, K -W., Gao, R., Park, H-G. ; Kim, S. ;  
448 Min, J.-E; Kang, S. C.; Guan, G. Light hydrocarbons to BTEX aromatics over

- 449 Zn-modified hierarchical ZSM-5 combined with enhanced catalytic activity  
450 and stability, *Micro. Meso. Mat.*, **2019**, 284, 316-326.
- 451 [8] Bartholomew, C.H. Mechanisms of catalyst deactivation, *Appl. Catal. A: Gen.*,  
452 **2001**, 212, 17-60.
- 453 [9] Seddon, D. Paraffin oligomerisation to aromatics, *Catal. Today*, **1990**, 6, 351-  
454 372.
- 455 [10] Roessner, F.; Hagen A.; Mroczek, U.; Karge, H.G.; Steinberg, K. H.  
456 Conversion of Ethane into Aromatic Compounds on ZSM-5 Zeolites Modified  
457 by Zinc Proceedings of the 10<sup>th</sup> international Congress on catalysis New  
458 frontiers in Catalysis, **1992**, part B, 1707.
- 459 [11] Guisnet, M.; Magnoux, P. Organic chemistry of coke formation, *Appl. Catal.*  
460 *A: Gen.*, **2001**, 212, 83-96.
- 461 [12] Guisnet, M.; Ribeiro, F. R. Deactivation and regeneration of zeolite catalysts,  
462 Imperial College Press, Series Editor G. J. Hutchings (2011).
- 463 [13] Asaftei, I. V.; Earar, K.; M. Birsa, L.; Sandu, I. G.; Lungu, N. C.; Sandu, I.  
464 Conversion of light hydrocarbons with butanes and butenes from petroleum  
465 refining processes over Zn-HZSM-5 and ZnO/ HZSM-5 catalysts, *Rev. Chim.*,  
466 **2015**, 66, 963-971.
- 467 [14] Miranda, C.; Ramírez, A.; Sachse, A.; Gaudin, P.; Pouilloux, Y.; Pinard, L.  
468 Exploring the impact of zeolite voids in liquid phase reactions : the case of  
469 glycerol etherification by tert-butyl alcohol. *J. Catal.*, **2018**, 307, 249-260.
- 470 [15] Pinard, L.; Hamieh, S.; Canaff, C.; Ferreira Madeira, F.; Batonneau-Gener, I.;  
471 Maury, S.; Delpoux, O.; Ben Tayeb K.; Pouilloux, Y.; Vezin, H. Growth

- 472 mechanism of coke on HBEA zeolite during ethanol transformation, *J. Catal.*  
473 **2013**, 299, 284-297.
- 474 [16] Biscardi, J. A.; Meitzner, G. D.; Iglesia, E. Structure and density of active Zn  
475 species in Zn/H-ZSM5 propane aromatization catalysts, *J. Catal.*, **1998**, 179,  
476 192-202.
- 477 [17] Batonneau-Gener, I.; Sachse. A. Determination of the exact microporous  
478 volume and BET surface area in hierarchical ZSM-5, *J. Phys. Chem. C*, **2019**,  
479 123, 7, 4235-4224.
- 480 [18] Zhang, Y.; Zhou, Y.; Huang, L.; Zhou, S.; Sheng, X.; Wang, Q.; Zhang, C.  
481 Structure and catalytic properties of the Zn-Modified ZSM-5 supported  
482 platinumium catalyst for propane dehydrogenation, *Chem. Eng. Jour.* **2015**, 270,  
483 352-361.
- 484 [19] Clatworthy, E. B.; Konnov, S. V.; Dubray,F.; Nesterenko N.; Gilson, J-P.;  
485 Mintova S. Emphasis on the properties of metal-containing zeolites operating  
486 outside the comfort zone of current heterogeneous catalytic reactions, *Angew.*  
487 *Chem. Int.*, **2020**, 59, 19414-19432.
- 488 [20] Konnov, S. V.; Dubray,F.; Clatworthy, E. B.; Kouvatas,C.; Gilson, J-P.; Dath,J -P.;  
489 Minoux, D.; Aquino, C.; Valtchev, V.; Moldovan, S.; Koneti, S.; Nesterenko, N.;  
490 Mintova. S. Novel strategy for the synthesis of ultra-stable single-site Mo-ZZSM-5  
491 zeolitenanocrystals, *Angew. Chem. Int.*, **2020**, 59, 19553-19560.
- 492 [21] Dufresne, L. A.; Le Van Mao, R.; Hydrogen back-spillover effects in the  
493 aromatization of ethylene on hybrid ZSM-5 catalysts. *Catal. Lett.*, **1994**, 25,  
494 371-383.

- 495 [22] Le van Mao, R.; Dufresne, L. A.; Yao, J.; Yu, Y. Effects of the nature of coke  
496 on the activity and stability of the hybrid catalyst used in the aromatization of  
497 ethylene and n-butane, *Appl. Catal. A: Gen.*, **1997**, *164*, 81-89.
- 498 [23] Arishtirova, K.; Dimitrov, C.; Dyrek, K.; Hallmeier, K.-Hz.; Popova, Z.;  
499 Witowski, S. Influences of copper on physico-chemical and catalytic properties  
500 of ZSM-5 zeolites in the reaction of ethane aromatization, *Appl. Catal.*, **1992**,  
501 *81*, 15-26.
- 502 [24] Qiu, P.; Lunsford, J. H.; Rosynek, M. P. Characterization of Ga/ZSM-5 for the  
503 catalytic aromatization of dilute ethylene streams, *Catal. Lett.*, **1998**, *52*, 37-42.
- 504 [25] Gao, J.; Wei, C.; Dong, M.; Wang, G.; Li, Z.; Qin, Z.; Wang, J.; Fan, W.  
505 Evolution of Zn species on Zn/HZSM-5 catalyst under H<sub>2</sub> pretreated and its  
506 effect on ethylene aromatization, *ChemCatChem* **2019**, *11*, 3892-3902.
- 507 [26] Ying, L.; Zhu, J.; Cheng, Y.; Wang, L.; Li, X. Kinetic modelling of C<sub>2</sub>-C<sub>7</sub>  
508 olefins interconversion over ZSM-5 catalyst, *J. Ind. Eng. Chem.* **2016**, *33*, 80.-  
509 90.
- 510 [27] Lukyanov, D. B. Development of kinetic models for reactions of light  
511 hydrocarbons over ZSM-5 catalysts. Experimental studies and kinetics  
512 modelling of ethane transformation and deactivation of HZSM-5 catalysts,  
513 *Stud. Surf. Sci. Catal.*, **1999**, *122*, 299-306.
- 514 [28] Wojciechowsky, B.M.. A theoretical treatment of catalyst decay, *Can. J. Chem.*  
515 *Eng.*, **1968**, *46*, 48-52.
- 516 [29] Marin, G .B.; Froment, G. F. Reforming of C<sub>6</sub> hydrocarbons on a P/Al<sub>2</sub>O<sub>3</sub>  
517 catalyst., *Chem. Eng. Sci.*, **1983**, *37*, 759-773.

- 518 [30] Jimenez-Garcia, G.; Aguilar-Lopez, R.; Leon-Becerril, E.; Maya-Yescas, R.  
519 Tracking catalyst activity during fluidized-bed catalytic cracking, *Ind. Eng.*  
520 *Chem. Res.*, **2009**, *48*, 1220-1227.
- 521 [31] Quintana-Solorzano, R.; Thybaut, J.W.; Galtier, P.; Marin, G.B. Simulation of  
522 an industrial riser for catalytic cracking in the presence of coking using single-  
523 event microkinetics, *Catal. Today*, **2010**, *150*, 319-331.
- 524 [32] Beirnaert, H. C.; Alleman, J.R.; Marin, G.B. A fundamental kinetic model for  
525 the catalytic cracking of alkanes on a USY zeolite in the presence of coke  
526 formation. *Ind. Eng. Chem. Res.*, **2001**, *40*, 1337-1347.
- 527 [33] Lakiss, L.; Ngoye, F.; Canaff, C.; Gilson, J-P, Laforge, S.; Qin, Z.; Tarighi,  
528 M.; Thomas, K.; Valtchev, V.; Vicente, A.; Pinard, L.; Fernandez, C. On the  
529 remarkable resistance to coke formation of nanometer-sized and hierarchical  
530 MFI zeolites during ethanol to hydrocarbons transformation, *J. Catal.*, **2015**,  
531 *328*, 165-172.
- 532 [34] Cerquiera, H. S.; Ayrault, P.; Datka, J.; Guisnet, M. Influence of coke on the  
533 acid properties of a USHY zeolite. *Mico. Meso. Mat.*, **2000**, *38*, 197-205.
- 534 [35] Astafan, A.; Benghalem, M.A.; Patarin, J.; Pouilloux, Y.; Bats, N.; Bouchy,  
535 C.; Pinard, L.; Daou, T.J. Particular properties of the coke formed on nano-  
536 sponge \*BEA zeolite during ethanol-to-hydrocarbons transformation, *J. Catal.*,  
537 **2016**, *336*, 1-10.
- 538 [36] Chaouati, N.; Soualah, A.; Chater, M.; Tarighi, M.; Pinard L. Mechanisms of  
539 coke growth on mordenite zeolite, *J. Catal.*, **2016**, *344*, 354-364.
- 540 [37] Guisnet, M.; Costa, L.; Ribeiro, F. R. Prevention of zeolite deactivation by  
541 coking, *J. Mol. Catal. A: Chem.*, **2009**, *305*, 69-83.

- 542 [38] Jia, L.Y.; Farouha, A.; Pinard L.; Hedan, S.; Comparot, J.-D.; Ben Tayeb, K.;
- 543 Dufour, A.; Vezin, H.; Batiot-Dupeyrat, C. New routes for complete
- 544 regeneration of coked zeolite, *Appl. Catal. B: Env.*, **2017**, 219, 82-91.
- 545 [39] Astafan, A.; Batiot Dupeyrat, C.; Pinard, L. Mechanism and kinetic of coke
- 546 oxidation by a non thermal plasma in a fixed bed dielectric barrier reactor
- 547 *J. Phys. Chem. C*, **2019**, 123, 9168-9175.
- 548

## Table and figure captions

- Table 1:** Comparison of Zn content and concentration of Brønsted and Lewis acid sites between fresh and spent catalysts.
- Table 2:** Acidic properties and Zn content of the 3,6 Zn40 catalyst after 1 and 2 reaction – regeneration cycles in ethylene transformation.
- Figure 1:** UV-visible spectra of catalysts series 40.
- Figure 2:** TEM images of bifunctional catalysts with a lower and higher metal content than the Zn exchange capacity.
- Figure 3:** IR spectra of OH region of the parent zeolite and relative intensities of bridged OH groups as a function of zinc content on 15, 40 In the presented spectra, the adsorbance was normalized to sample wafer density ( $\text{g cm}^{-2}$ ).
- Figure 4:** Concentrations of Brønsted acid sites (a) and Lewis acid sites (b) as a function of Zn content. (c) Stoichiometry of the transformation of BAS into LAS by Zn impregnation
- Figure 5:** Ethylene conversion as a function of the time-on stream on 15, 40 and 75 catalyst series.
- Figure 6:** Deactivation constant as a function of the concentration of the Lewis Zn (a) and Brønsted (b) acid sites and of the molar ratio  $\text{Zn}_{\text{Lewis}}/\text{H}^+$  (c).
- Figure 7:** Residual activity after 280 min as a function of concentration of Brønsted acid sites (a) and weight content of active zinc species (b). and of the molar ratio  $\text{Zn}_{\text{Lewis}}/\text{H}^+$  (c)
- Figure 8:** Coke content as function of time-on-stream (a), and deactivation function of 3.4Zn15 catalyst vs coke content (b) (open symbol : coke content minus that formed on HZ15 zeolite).
- Figure 9:** Deactivation function of 3.4Zn15 catalyst as a function of the catalyst coke content (full symbol) and coke content minus that formed on HZ15 zeolite (open symbol).
- Figure 10:** Losses of Brønsted (black symbol) and Lewis (blue symbol) acid sites and micropore volumes (red symbol) on the 3.4Zn15 catalyst as a function of time (a) and coke content (b).
- Figure 11:** Molar yields of hydrogen, methane, ethane, propylene, butenes and aromatics as a function of the initial conversion (black symbol) and after 280 min (red symbol).
- Figure 12:** Coke content as a function of initial yield into aromatics on the three catalyst series
- Figure 13:** Bands of coke molecules in regions  $3200\text{-}2800\text{ cm}^{-1}$  as a function of zinc content on 15, 40 and 75 catalyst series (dashed line = HZ catalysts).
- Figure 14:** Bands of coke molecules in region  $1700\text{-}1300\text{ cm}^{-1}$  as a function of zinc content on 15, 40 and 75 catalyst series (dashed line = HZ catalysts).
- Figure 15:** Volume apparently occupied by coke as a function of its content (a) and of volume that it really occupies (b), and residual activity between the residual micropore volume (c)
- Figure 16:** Proportion of Brønsted (a) and Lewis (b) acid sites neutralized as a function of coke content and residual activity after 280 min as a function of the proportion of Brønsted (c) and Lewis (d) acid sites neutralized.
- Figure 17:** Oxidation temperature at which 50% (black symbol) and 90% (red symbol) of coke is burned as a function of concentration of Brønsted (b) and Lewis Zn (a) acid sites, the molar ratio  $\text{Zn}_{\text{Lewis}}/\text{H}^+$  (c), micropore volume of the spent catalyst (d) and coke content (e).
- Figure 18:** Reaction– regeneration cycles in ethylene transformation on 3.6Zn40.

**Table 1.** Comparison of Zn content and concentration of Brønsted and Lewis acid sites between fresh and spent catalysts

Series	Catalyst <sup>a</sup>	Fresh					k <sub>D</sub>	Spent after 280 min				
		Zn/Al <sup>a</sup>	[H <sup>+</sup> ] <sup>b</sup>	[L] <sup>c</sup>	[Zn <sub>LEWIS</sub> ]/[H <sup>+</sup> ]	V <sub>micro</sub>		Coke <sup>d</sup>	Zn <sup>a</sup>	[H <sup>+</sup> ] <sup>b</sup>	[L] <sup>c</sup>	V <sub>micro</sub>
	wt. %	mol/mol	μmol g <sup>-1</sup>	mol/mol	mol/mol	cm <sup>3</sup> g <sup>-1</sup>	s <sup>-1</sup> g <sup>-1</sup> (x 10 <sup>3</sup> )	wt. %	wt. %	μmol g <sup>-1</sup>	cm <sup>3</sup> g <sup>-1</sup>	
15	HZ15	-	515	44	0	0.139	0.033	1.4	-	444	103	0.138
	0.7Zn15	0.3	364	346	0.4	0.150	0.075	1.9	-	279	357	0.123
	2.0Zn15	0.3	201	671	1.5	0.147	0.308	6.2	-	71	387	0.063
	3.4Zn15	0.5	144	792	2.6	0.140	0.500	6.8	-	30	153	0.026
	4.1Zn15	0.6	121	688	3.2	0.132	0.725	6.7	-	39	237	0.053
	8.1Zn15	1.2	84	655	5.1	0.130	1.220	7.5	-	29	78	0.014
40	HZ40	-	286	28	0	0.171	0.008	2.3	-	218	39	0.135
	0.5Zn40	0.2	229	176	0.2	0.179	0.033	2.9	0.5	136	213	0.130
	0.8Zn40	0.3	217	253	0.3	0.176	0.092	3.9	1.0	76	288	0.106
	1.4Zn40	0.5	199	329	0.5	0.171	0.875	5.0	1.5	58	353	0.098
	2.1Zn40	0.7	163	367	0.7	0.165	0.192	6.6	2.0	54	266	0.072
	3.6Zn40	1.3	77	399	2.7	0.147	0.492	4.8	3.9	60	477	0.107
75	5.6Zn40	1.8	100	443	1.9	0.143	0.525	5.3	-	35	268	0.090
	HZ75	-	148	21	0	0.151	0.005	0.9	-	175	25	0.136
	0.3Zn75	0.2	111	67	0.3	0.140	0.025	1.5	-	68	115	0.138
	0.7Zn75	0.4	92	98	0.6	0.145	0.142	2.0	-	39	137	0.116
	2.7Zn75	1.6	84	102	0.8	0.142	0.200	2.4	-	25	146	0.118

<sup>a</sup> = Zn content measured by ICP analysis, <sup>b,c</sup> = concentrations of Brønsted and Lewis acid sites probed by thermodesorption of pyridine at 150°C. <sup>d</sup> = measured by thermogravimetry analysis

**Table 2.** Acidic properties and Zn content of the 3,6 Zn40 catalyst after 1 and 2 reaction – regeneration cycles in ethylene transformation.

State	Zn <sup>a</sup> wt. %	[PyH <sup>+</sup> ] <sup>b</sup> μmol g <sup>-1</sup>	[PyL] <sup>c</sup> μmol g <sup>-1</sup>
Fresh	3.6	77	399
Regenerated x1		108	356
Regenerated x2	3.4	69	261

<sup>a</sup> = Zn content measured by ICP analysis, <sup>b,c</sup> = concentrations of Brønsted and Lewis acid sites probed by thermodesorption of pyridine at 150°C.

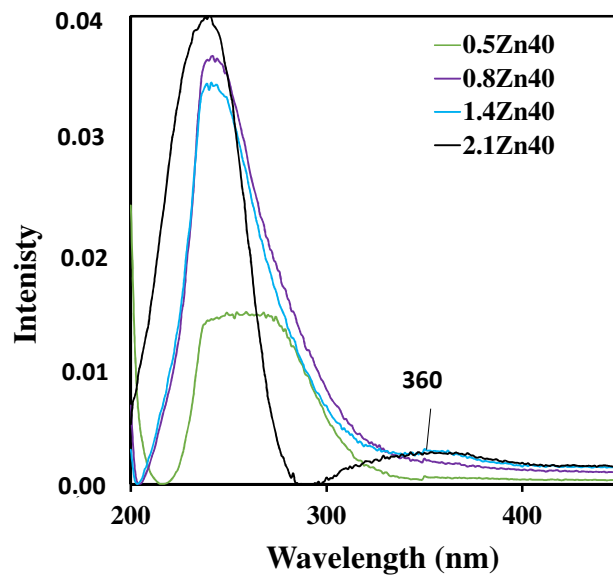


**Figure 1:** UV-visible spectra of catalysts series 40.

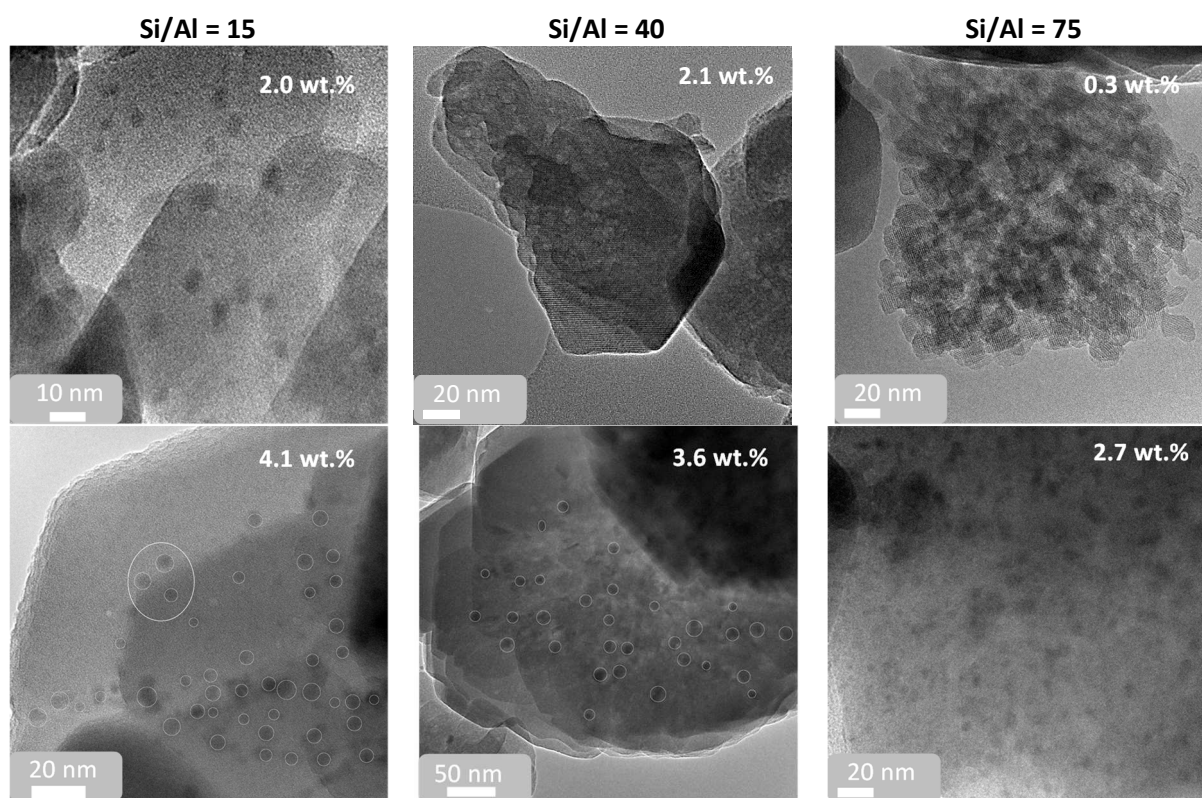


**Figure 2:** TEM images of bifunctional catalysts with a lower and higher metal content than the Zn exchange capacity.

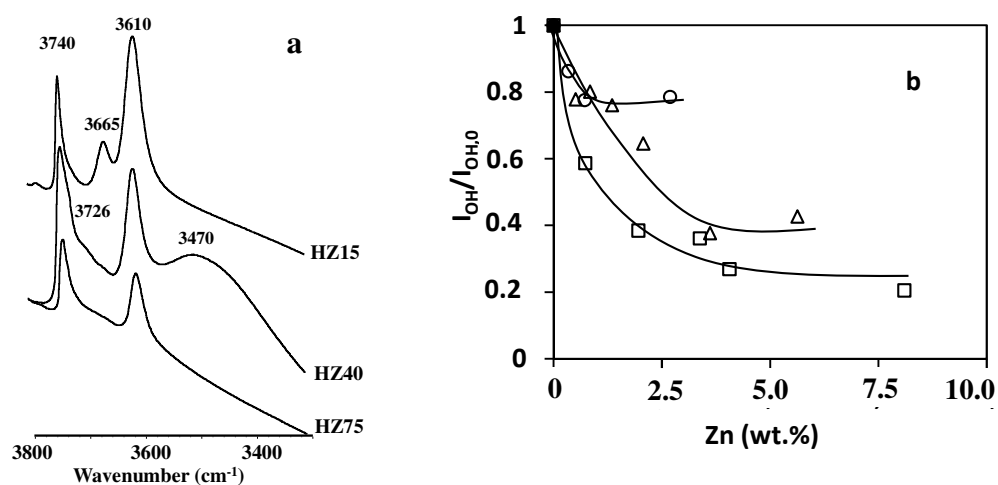


**Figure 3:** IR spectra of OH region of the parent zeolites and relative intensities of bridged OH groups as a function of zinc content on 15, 40 In the presented spectra, the adsorbance was normalized to sample wafer density ( $\text{g cm}^{-2}$ ).

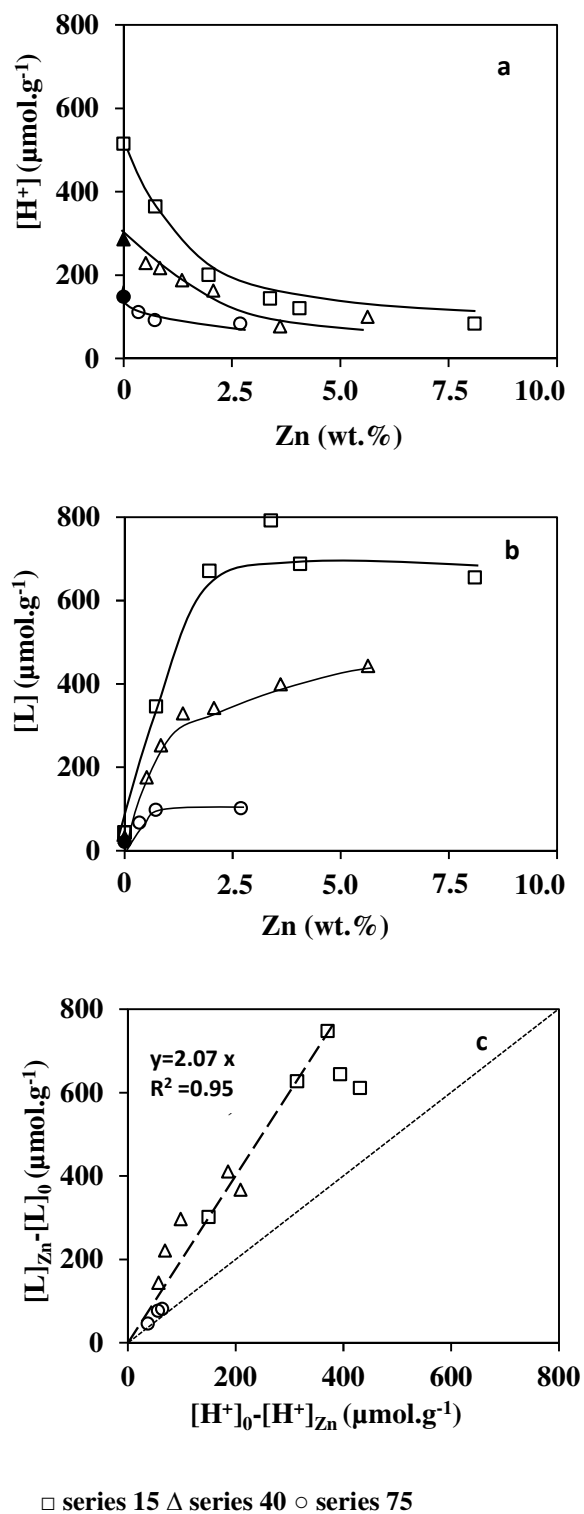


**Figure 4:** Concentrations of Brønsted acid sites (a) and Lewis acid sites (b) as a function of Zn content. (c) Stoichiometry of the transformation of BAS into LAS by Zn impregnation

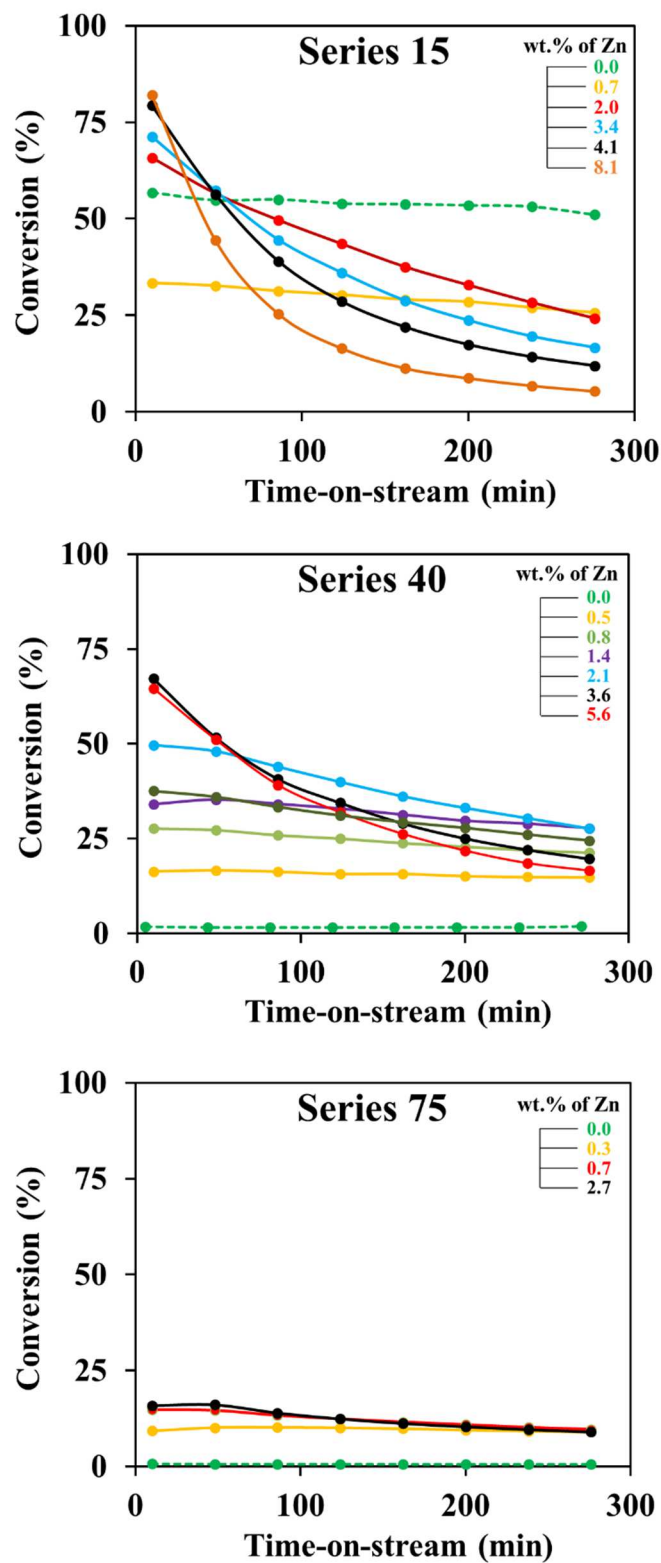


**Figure 5:** Ethylene conversion as a function of the time-on stream on 15, 40 and 75 catalyst series.

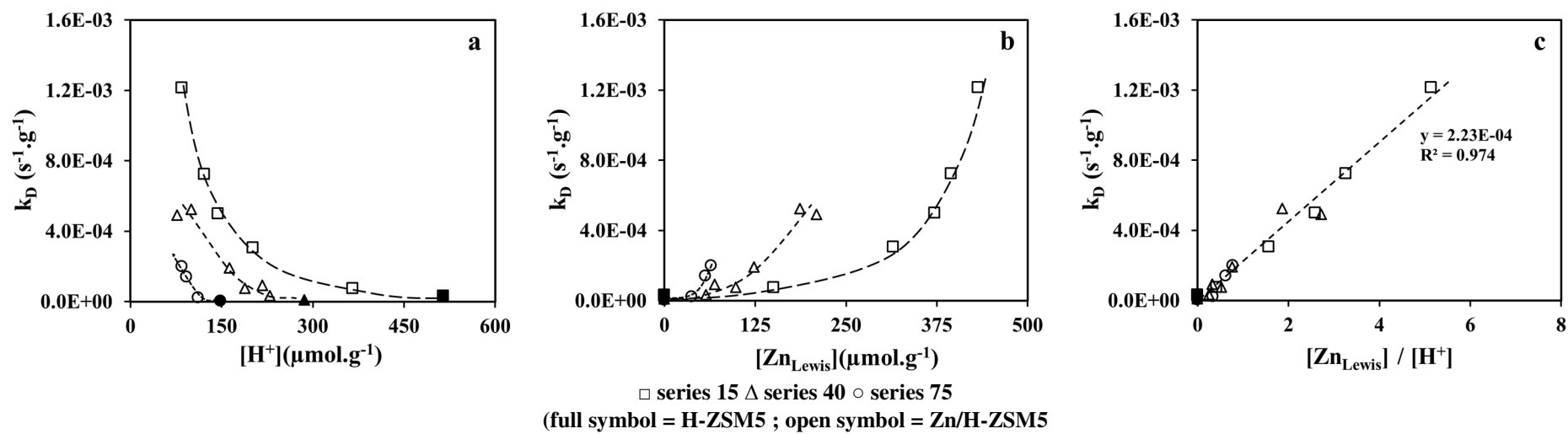


**Figure 6.** Deactivation constant as a function of the concentration of Brønsted (b) and Lewis Zn (a) acid sites and the molar ratio  $Zn_{Lewis}/H^+$  (c).

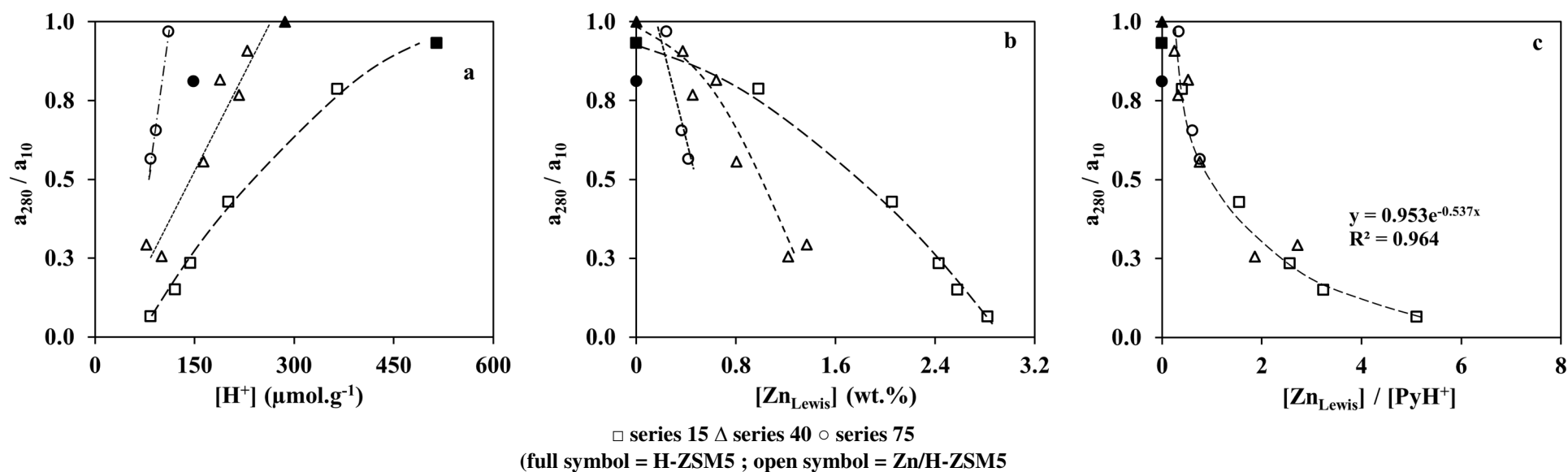


**Figure 7:** Residual activity after 280 min as a function of concentration of Brønsted acid sites (a) and weight content of active zinc species (b) and the molar ratio of concentration of active Zinc species to Brønsted acid sites (c).

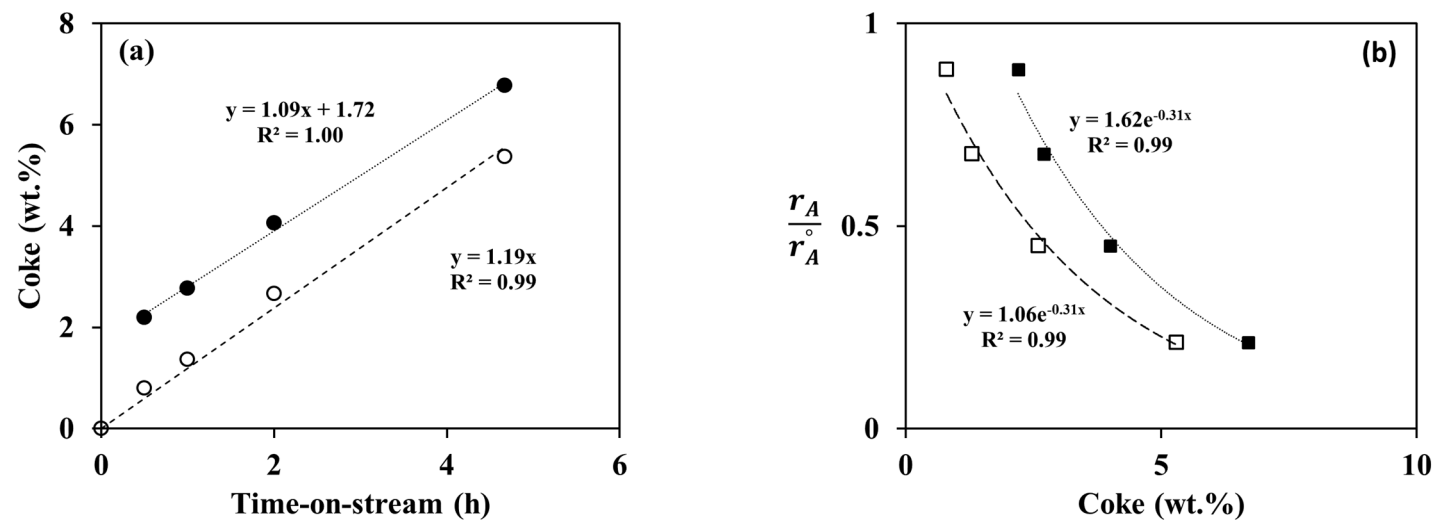


**Figure 8:** Coke content as function of time-on-stream (a), and deactivation function of 3.4Zn15 catalyst vs coke content (b) (open symbol : coke content minus that formed on HZ15 zeolite).

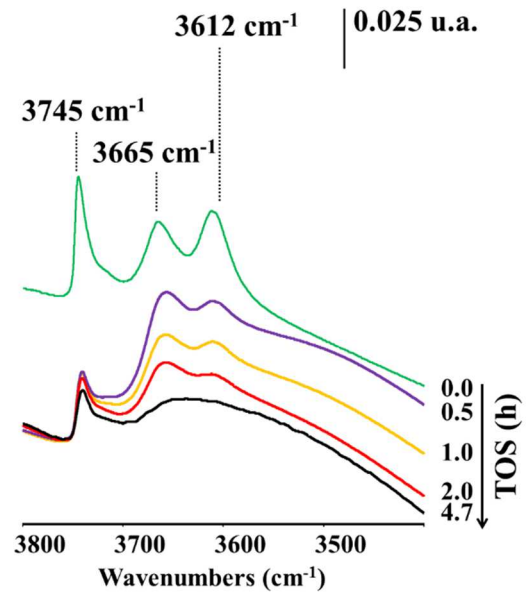


**Figure 9:** IR spectra of OH region of 3.4Zn15 after different times-on-stream. In the presented spectra, the adsorbance was normalized to sample wafer density (g cm<sup>-2</sup>).

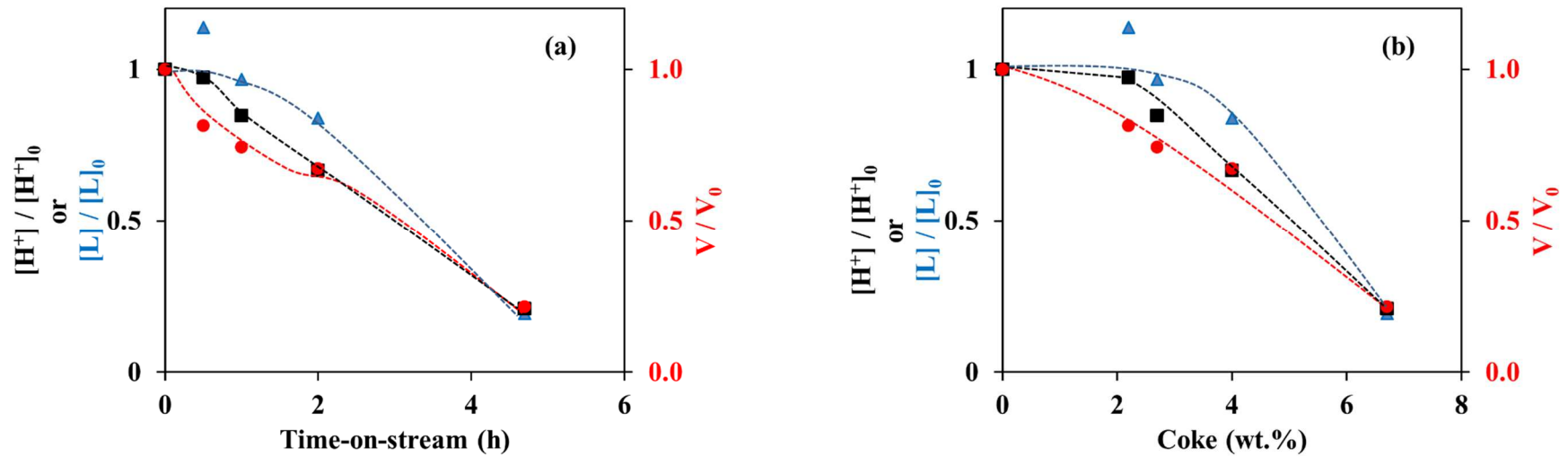


**Figure 10:** Losses of Brønsted (black symbol) and Lewis (blue symbol) acid sites and micropore volumes (red symbol) on the 3.4Zn15 catalyst as a function of time (a) and coke content (b).

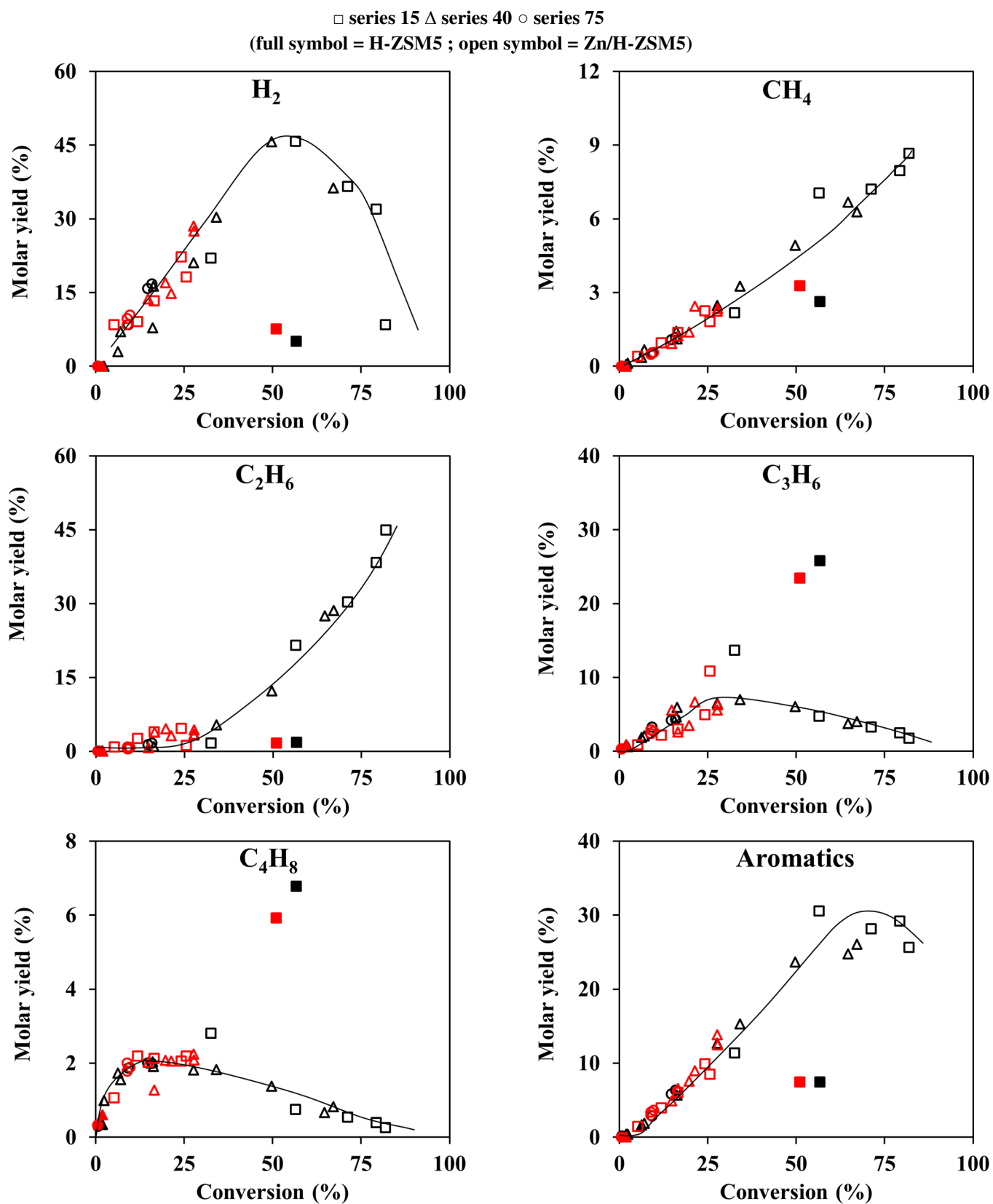


**Figure 11:** Molar yields of hydrogen, methane, ethane, propylene, butenes and aromatics as a function of the initial conversion (black symbol) and after 280 min (red symbol).

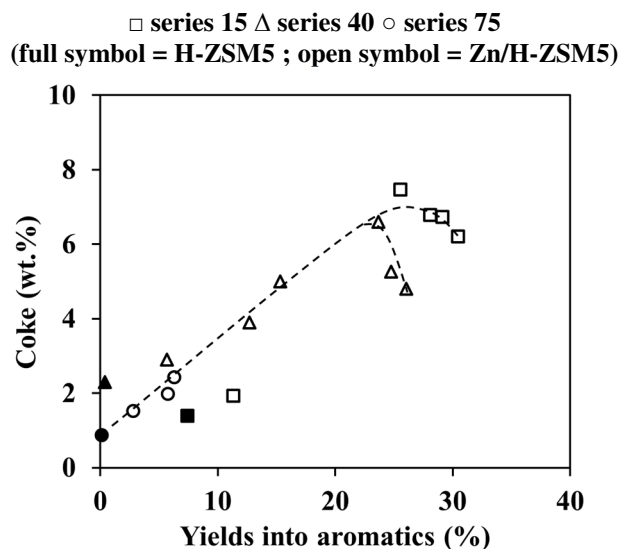


**Figure 12:** Coke content as a function of initial yield into aromatics on the three catalyst series.

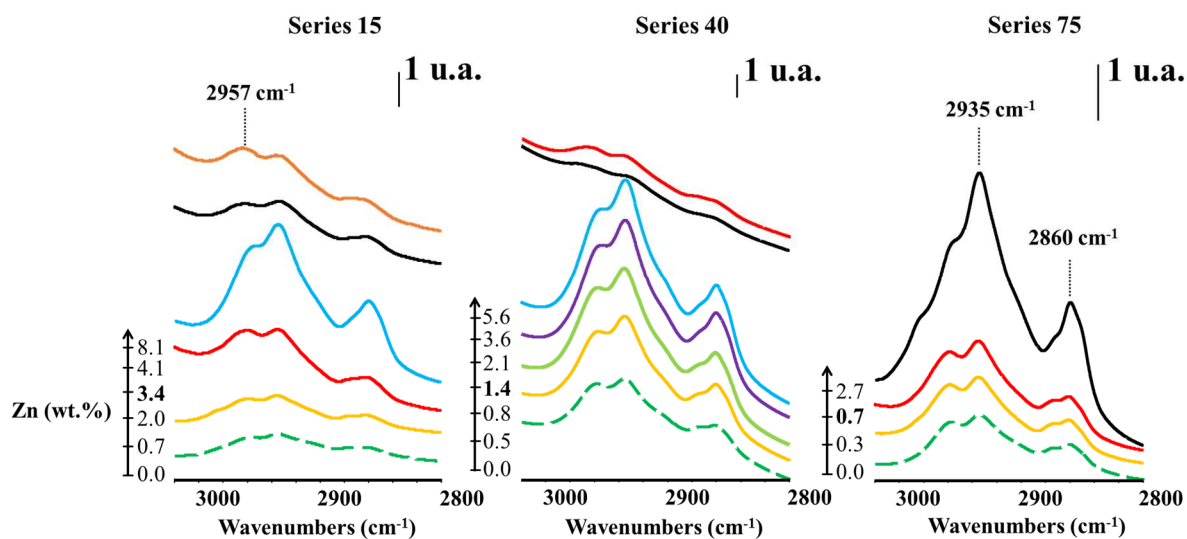


**Figure 13:** Bands of coke molecules in region 3020-2800  $\text{cm}^{-1}$  as a function of zinc content on 15, 40 and 75 catalyst series (dashed line = HZ catalysts).

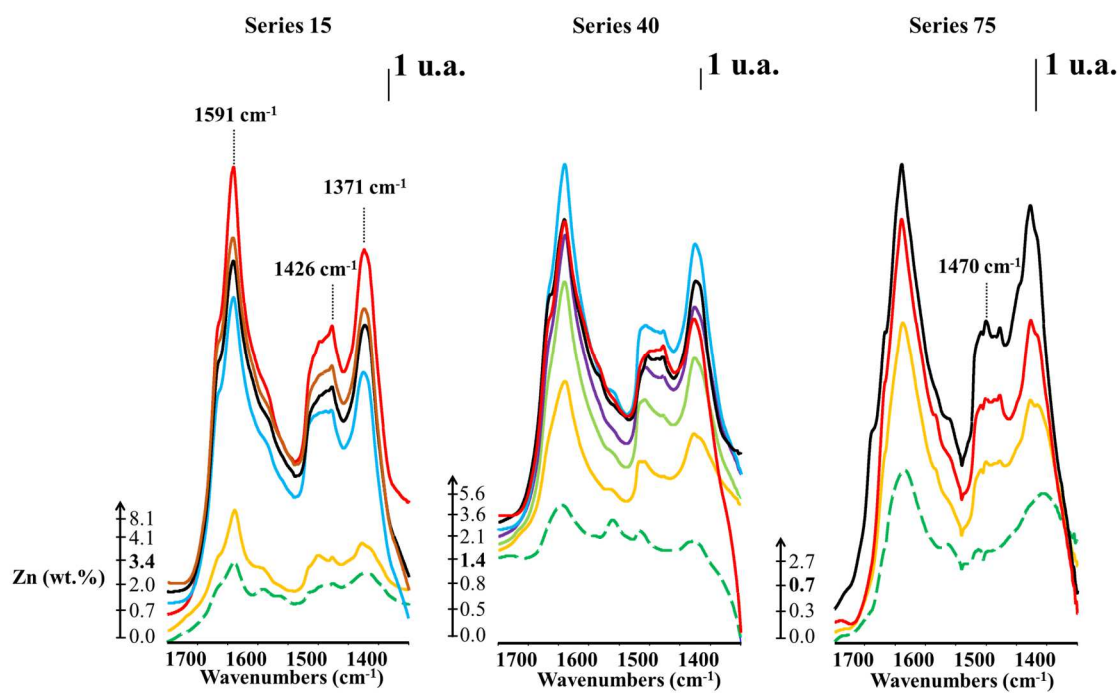
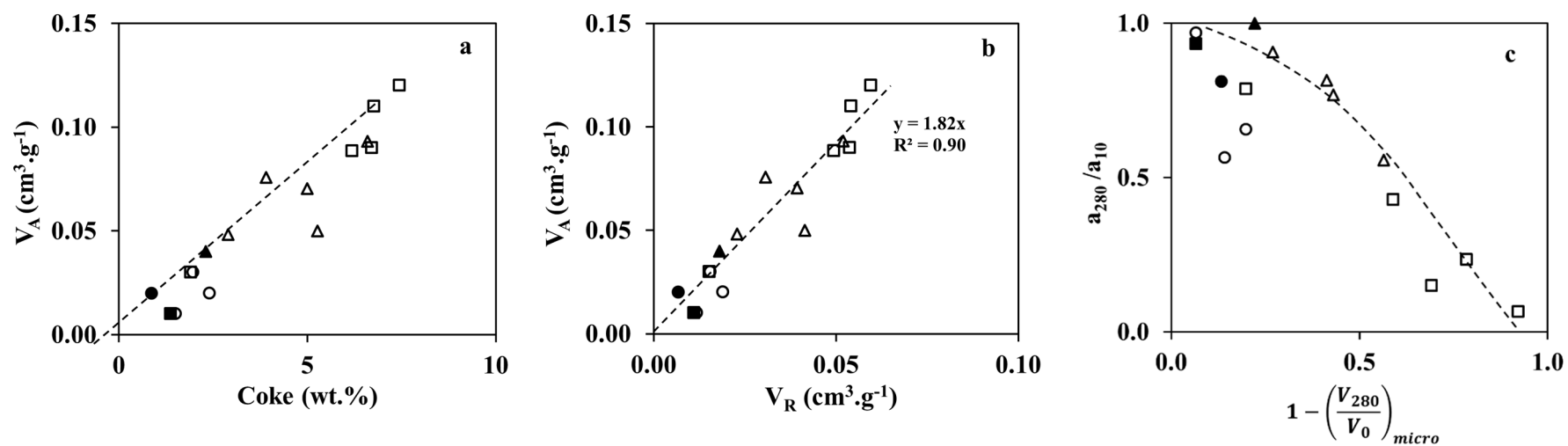


**Figure 14:** Bands of coke molecules in region 1800-1300  $\text{cm}^{-1}$  as a function of zinc content on 15, 40 and 75 catalyst series (dashed line = HZ catalysts).



□ series 15 △ series 40 ○ series 75  
 (full symbol = H-ZSM5 ; open symbol = Zn/H-ZSM5)

**Figure 15:** Volume apparently occupied by coke as a function of its content (a) and of volume that it really occupies (b), and residual activity between the residual micropore volume (c).

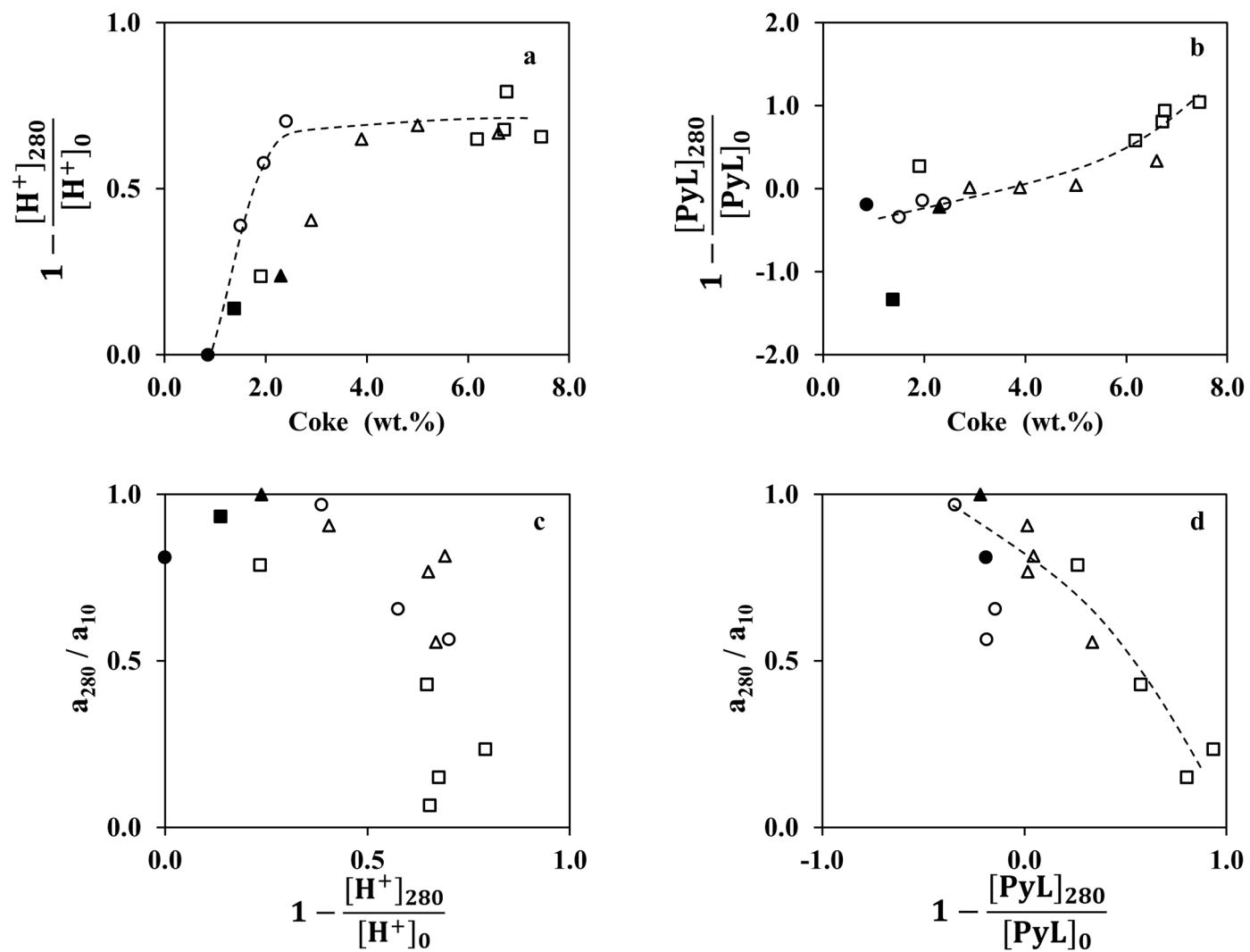


**Figure 16:** Proportion of Brønsted (a) and Lewis (b) acid sites neutralized as a function of coke content and residual activity after 280 min as a function of the proportion of Brønsted (c) and Lewis (d) acid sites neutralized.

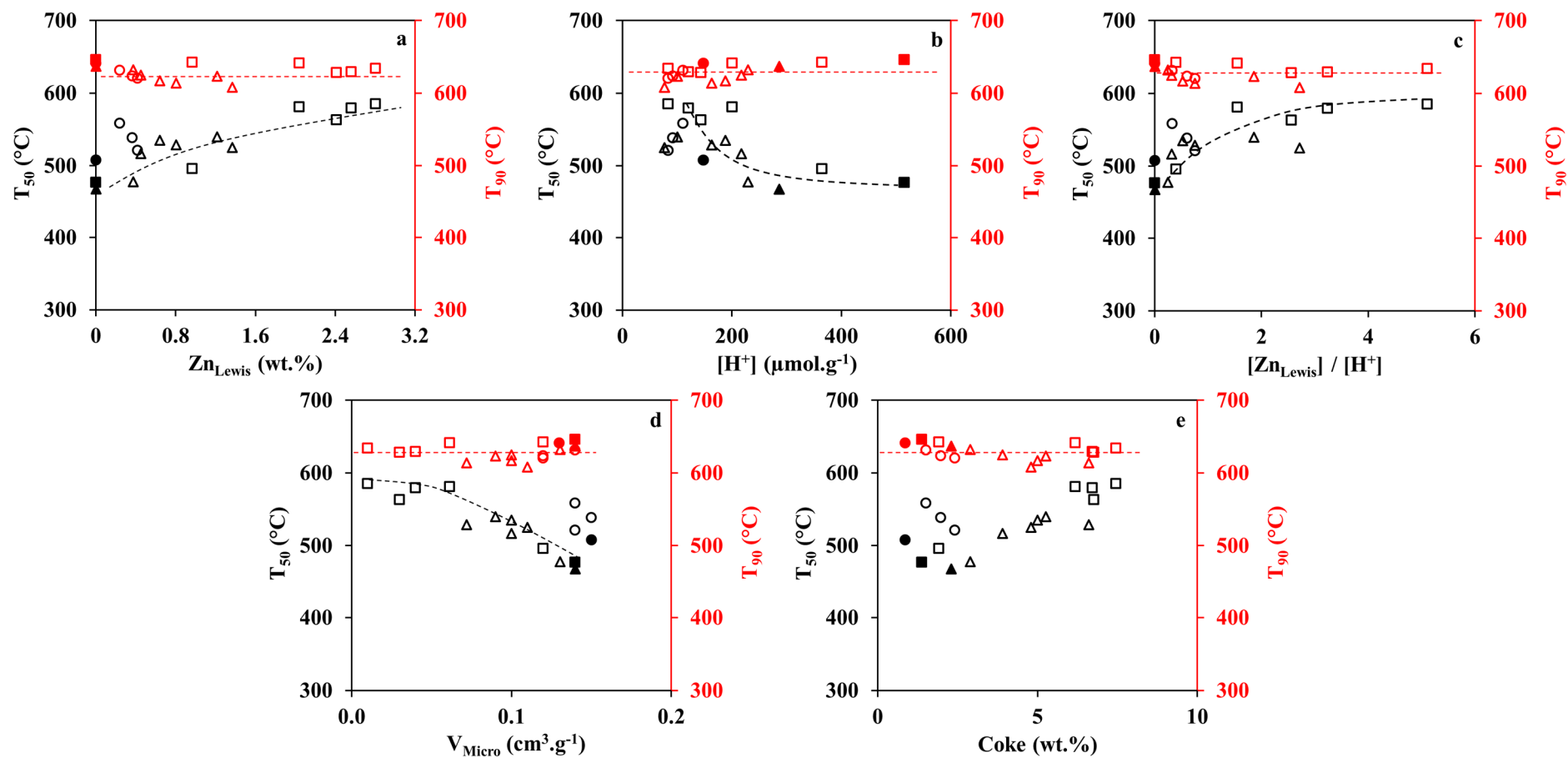


**Fig. 17:** Oxidation temperature at which 50% (black symbol) and 90% (red symbol) of coke is burned as a function of concentration of Brønsted (b) and Lewis Zn (a) acid sites, the molar ratio  $Zn_{Lewis}/H^+$  (c), micropore volume of the spent catalyst (d) and coke content (e).

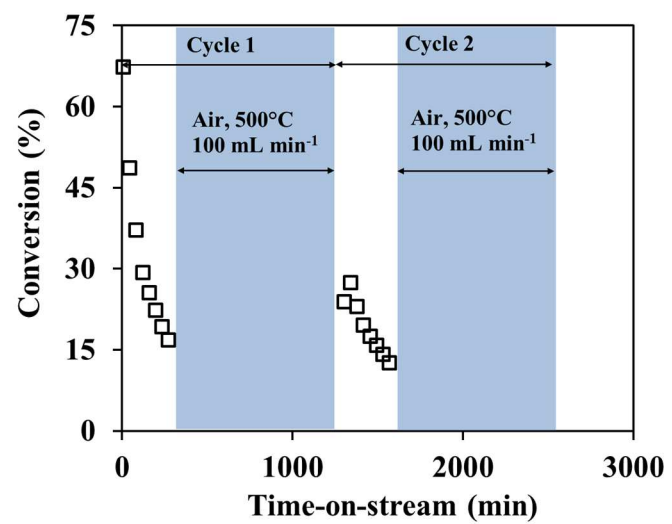


**Fig. 18.** Reaction– regeneration cycles in ethylene transformation on 3.6Zn40.

